International Journal of Innovative Computing, Information and Control
Volume **19**, Number **1**, February **2023**

 ISSN 1349-4198
pp. 1–14

AUTOMATIC IDENTIFICATION OF TUMOR CELLS FOR CIRCULATING TUMOR CELLS BY CONVOLUTIONAL NEURAL NETWORKS

Kazuki Hashimoto[1], Tohru Kamiya[1], Guangxu Li[2], Kazue Yoneda[3,4] and Fumihiro Tanaka[4]

[1]Department of Mechanical and Control Engineering
Kyushu Institute of Technology
1-1, Sensui, Tobata, Kitakyushu, Fukuoka 804-8550, Japan
kamiya@cntl.kyutech.ac.jp

[2]School of Electronics and Information Engineering
Tiangong University
No. 399, Binshuixi Road, Xiqing District, Tianjin 300387, P. R. China
liguangxu@tiangong.edu.cn

[3]Department of Omics Medicine
Hyogo Medical University
1-1, Mukogawa, Nishinomiya, Hyogo 663-8501, Japan
kyoneda@hyo-med.ac.jp

[4]Second Department of Surgery (Chest Surgery)
University of Occupational and Environmental Health
1-1, Iseigaoka, Yahatanishi, Kitakyushu, Fukuoka 807-8555, Japan
ftanaka@med.uoeh-u.ac.jp

Received May 2022; revised September 2022

Abstract. *Liquid biopsy allows non-invasive collection of circulating tumor cells (CTCs) in blood without the need for sampling and can clearly demonstrate their presence in many types of cancer. In this study, we propose a method to automatically identify CTCs from fluorescence microscopy images and enable quantitative analysis based on convolutional neural networks (CNN). In this paper, a cell nucleus region cropping algorithm is applied in addition to a filtering process centered on a selective enhancement filter. Next, identification by SqueezeNet is performed. We performed the proposed method to 5,040 images of 6 samples and conducted experiments to identify CTCs. The number of detected CTCs was 148 (TPR = 100%), and the number of over-detected non-CTCs was 925. For the identification, TPR = 88.51% and FPR = 5.102% for the CNN model using SqueezeNet. The proposed method successfully reduced the number of detections by about 71.4% without missing any correct answers, but the proposed method did not show good results in any of the evaluation metrics.*

Keywords: Circulating tumor cells, Computer aided diagnosis, Cell nucleus, Convolutional neural network, SqueezeNet

1. **Introduction.** According to a WHO study, cancer is currently the leading cause of death in the world, accounting for about 10 million deaths in 2020 [1]. Since cancer progresses with repeated metastasis, early detection and treatment are important. Cancer can be diagnosed by imaging, biopsy, and endoscopy. A combination of these tests can provide a more accurate picture of the disease, but it is difficult to diagnose whether the cancer has metastasized or not. In addition, due to the invasive nature of the test, it

DOI: 10.24507/ijicic.19.01.1

cannot be performed frequently for follow-up [2]. Therefore, in recent years, the blood test for circulating tumor cells (CTCs) has been attracting attention as a new biomarker.

CTC is a type of cells that can cause cancer metastasis and exist in the peripheral blood of cancer patients. By means of existence of the CTCs in blood, it enables early diagnosis of the metastatic cancer [3-5]. In the examination method, blood collected from the patient is injected into a chip and photographed, and imaging diagnosis is performed by a pathologist. Now, a device called Universal CTC-Chip has been developed to capture target cells in blood such as CTCs [6,7].

The Universal CTC-Chip is a chip with more than 30,000 microscopic protrusions called microposts on its surface. By coating the microposts with any antibody, it is possible to target and supplement various cells in the blood. CTCs need to be identified from a huge number of leukocytes via immunofluorescent labeling underlying the microscopy. In this study, we use the reaction of fluorescence coloration of three different substances to detect CTCs. the fluorescence reaction pattern of CTCs is "cytokeratin positive in red image, leukocyte negative in green image, cell nucleus positive in blue image".

The Universal CTC-Chip is expected to enable highly accurate capture of CTCs and improve diagnostic accuracy. However, identification of the CTCs population is a challenging problem. Since the low quantity of CTCs existing in a patient's peripheral blood and heterogeneity in the characteristics of CTCs [8], there is concern about an increased burden on the adjudicator. In addition, the identification results depend on the subjective judgment and experience of the judges. Locating specific target cells such as CTCs often requires tedious procedures. Therefore, the Computer Aided Diagnosis (CAD) system, a method in which physicians use the results of automatic computer analysis as a second opinion for diagnosis, has been attracting attention [9]. Various approaches to automatically identifying CTCs assisted by CAD systems have been proposed [10-12]. However, there is still lack of the research of CTCs on the Universal CTC-Chip. Therefore, new detection and identification algorithms for CTCs using Universal CTC-Chip are required.

Machine learning (ML) is a superior tool for developing automated processes of classification, which has been widely used to analyze CTCs nowadays [13-15]. However, machine learning methods output engineer-dependent results because the engineer selects the features to be used for identification, and there is a problem of not being able to respond to new cases. In recent years, methods based on deep learning have been attracting attention. Compared to classical machine learning approaches, deep learning can handle new cases because the computer automatically extracts features for identification. Convolutional neural network (CNN) is a new deep learning framework that can automatically learn to extract features and has been applied to various fields, including cell classification in the medical field [16-23]. Chen et al. used CNN to integrate features with high-throughput quantitative imaging enabled by Doppler effect, achieving high accuracy in label-free cell classifications [24].

In previous studies on automatic detection of CTCs using the Universal CTC-Chip, Nakamichi et al. proposed a detection method mainly based on filtering [25-27]. In the previous method [27], filtering was applied only to cytokeratin and identification was performed by CNN. However, since the detection of cell candidate regions was performed only for cytokeratin, 3,238 over-detected non-CTCs remained for 148 CTCs, and further reduction of over-detected non-CTCs detections and improvement of identification accuracy are required. Therefore, we proposed an automated method to detect CTCs from fluorescence microscopy images by not only focusing on cytokeratin but also identifying only cell nuclei. In this study, we aimed to develop an automated tool to detect CTCs accurately and efficiently from images acquired from the Universal CTC-Chip. To identify CTCs from 5,040 images of 6 samples, a new hybrid framework was implemented by

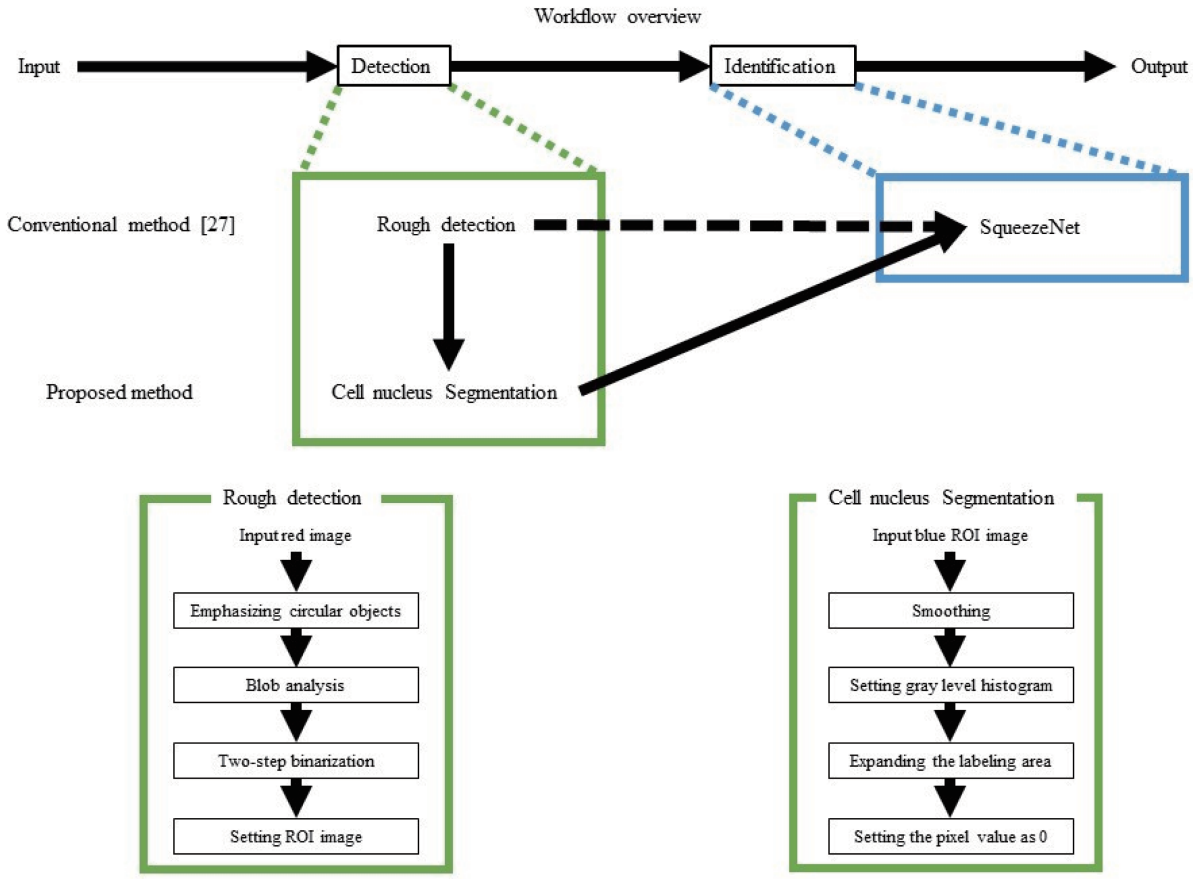

FIGURE 1. Flow chart of the proposed method

modifying the conventional method [27] and further identifying CTCs using CNN. Figure 1 shows the flow chart of the proposed method. In the detection phase of Figure 1, the dotted arrows represent the conventional method [27] and the solid arrows represent the proposed method.

2. **Preliminaries.**

2.1. **Materials and preprocessing.**

Cytokeratin in red image, Leukocyte in green image, and Cell nucleus regions in blue image are fluoresced by the microscope to produce fluorescence microscope images. Therefore, three types of images, red, green, and blue, are generated on the same coordinates of the Universal CTC-Chip. Here, an inverted microscope DMi8 from Leica [28] was used in this study. We have prepared 5,040 images for 6 samples. They are also used under the same conditions in the methods of Nakamichi et al. [27]. Then, the candidate cell regions were detected by the proposed method and identified by CNN [29].

2.2. **Point detection.**

Point selective enhancement filter is a filter that adapts to the noise components and scale changes in the images [30]. The point selective enhancement filter is obtained by the following equation,

$$z(\lambda_1, \lambda_2) = \begin{cases} \dfrac{|\lambda_2|^2}{|\lambda_1|} & \text{if } \lambda_1 < 0,\ \lambda_2 < 0 \\ 0 & \text{otherwise} \end{cases} \tag{1}$$

where λ_1 and λ_2 show the eigenvalues of the Hessian matrix.

Here, we assume that the diameter of the object to be emphasized is from d_0 to d_1. First, smoothing by a Gaussian filter with a scale of $\sigma = d_0/4$ is applied to the two-dimensional image f to get the smoothed image g. Then, the above-mentioned point selective enhancement filter is applied to this smoothed image g. The process above is repeatedly applied N times until $\sigma = d_1/4$ with increasing σ. Each scale can be obtained by the following equation,

$$\sigma_N = r^{N-1}\sigma_1 \tag{2}$$

$$r = \left(\frac{d_1}{d_0}\right)^{\frac{1}{N-1}} \tag{3}$$

In this paper, the minimum diameter is $d_0 = 9$, the maximum diameter is $d_1 = 33$, and the point selective enhancement filter is applied by changing the radius for $N = 5$ iterations. These values are obtained experimentally, and this filter is also used under the same conditions in the methods of Nakamichi et al. [27].

2.3. **Blob analysis.** A series of connected elements in a binary image is called a blob. By reading the shape features of each blob in the image, we can estimate what the object is. Since cells are basically circular in shape, blob analysis can be used to extract only cell-like shapes. In this paper, we carry out blob analysis [31] by labeling the binarized image and calculating the geometric feature parameter for each labeled blob. The geometric feature parameters used in this paper are area S, circularity $F_{circularity}$, inertia ratio $F_{inertiaratio}$, and convexity $F_{convexity}$. Each geometric feature parameter can be obtained by the following equation,

$$F_{circularity} = \frac{4\pi S}{L^2} \tag{4}$$

$$F_{inertiaratio} = \frac{I_{\min}}{I_{\max}} \tag{5}$$

$$I_{\min} = \sqrt{2} \times \sqrt{\mu_{20} + \mu_{02} - \sqrt{(\mu_{20} - \mu_{02})^2 + 4\mu_{11}^2}} \tag{6}$$

$$I_{\max} = \sqrt{2} \times \sqrt{\mu_{20} + \mu_{02} + \sqrt{(\mu_{20} - \mu_{02})^2 + 4\mu_{11}^2}} \tag{7}$$

$$F_{convexity} = \frac{S}{S_{conv}} \tag{8}$$

where S is the area, L is the perimeter, $I_{\min}$ is the length of the coaxial axis, $I_{\max}$ is the length of the principal axis, μ_{20}, μ_{02}, μ_{11} are the normalized second moment of gravity, and S_{conv} is the area of the convex hull.

3. Method.

3.1. **Detection of cell candidates.** The flow of detection of cell candidate regions is shown in lower left of Figure 1. The first step of the detection is the coarse extraction of cell candidate regions by processing the entire red image. Then, ROIs (Region of Interest) were set around the extracted regions, and the final cell candidate regions were detected by processing the ROIs. In this paper, as in the methods of Nakamichi et al. [27], we mainly used red images. The reason for this is that red images have higher contrast and clearer boundaries than images in other channels, and there are fewer cells to react to. The detection of cell candidate regions is described in detail below.

At the first, a grayscale image of a red image was used as input, and a selective enhancement filter was applied to the input. Since cells are basically circular in shape, the selective

enhancement filter can be used to emphasize the point component, thereby emphasizing only the cell region, and suppressing the background component.

Secondly, blob analysis was performed after binarization with a threshold value from 1 to 10. This was done to degrade the information of the cell fragments, because the point selection enhancement filter alone emphasizes not only the cells but also the cell fragments. In half of the 10 binarized images, regions satisfying the four shape feature parameter conditions were detected as cell candidate regions. This process can stably extract regions with cell-like shapes at multiple thresholds in the grayscale image after enhancement and remove other regions as noise. The range of feature conditions was set as follows: area: $[40, 400]$, circularity: $[0.6, 1.0]$, inertia ratio: $[0.3, 1.0]$, convexity: $[0.7, 1.0]$. This is the same as the method of Nakamichi et al. [27]. All 64×64 pixel ROIs were set around the extracted region.

Thirdly, a two-step binarization process was performed. The Otsu's method was used for binarization. By using the discriminant analysis method in two stages of binarization, it is possible to correctly detect cell candidate regions even for fait cells. After that, the binarized image with an area of less than 10 pixels, more than 400 pixels, or a circularity of less than 0.5 was regarded as noise and denoised. Finally, ROIs of 32×32 pixels were cut out from each of the red, green, and blue images using the center-of-gravity coordinates corresponding to the obtained ROIs.

In this paper, we added the identification of cell nucleus to the above process. The flow of the identification of cell nucleus is shown in right lower of Figure 1. First, we applied a 3×3 average filter to the ROI of the blue image representing the cell nucleus to remove the noise. The mean filter used in this paper is expressed by the following equation,

$$K = \frac{1}{3 \times 3} \begin{bmatrix} 1 & 1 & 1 \\ 1 & 1 & 1 \\ 1 & 1 & 1 \end{bmatrix} \tag{9}$$

Next, gray level histogram was created for each ROI. From the smoothed image, the pixel value of each pixel was obtained, and the value was stored in the gray level histogram in the range of 0 to 255. Then, the largest pixel value was obtained from the gray level histogram, and one coordinate with that pixel value was obtained by raster operation [32]. Once the coordinate with the largest pixel value was obtained, the region was expanded from that coordinate to identify the shape of each cell nucleus. There were 8 directions in which the region was expanded: up, down, left, right, top right, top left, bottom left, and bottom right. The cell nucleus is basically circular in shape, and the pixel values are larger toward the center of the cell nucleus and smaller toward the outside. In the case of overlapping cell nucleus, the concentration value continues to decrease slowly from the center to the overlapping area, and the pixel value increases again after the overlapping area. Figure 2 shows an example of an extended region of a cell nucleus. In Fugure 2, the gray area represents the coordinate with the largest pixel value, the area at the root of the arrow represents the coordinate for area expansion, and the area pointed to by the arrow represents the coordinate used to determine area expansion. The condition for region expansion is whether the concentration value of the coordinate in the center of the cell nucleus is greater than the concentration value of the outer coordinate for all arrow directions in each case shown in the figure. If this condition is satisfied, then the target pixel is added as part of the cell nucleus, and if the condition is not satisfied, then the pixel is not a cell nucleus. Thus, for each of the directions shown in Figure 2, we introduce a process that continues to expand the region in concentric circles, starting from the coordinate closest to the coordinate with the largest concentration value, until there is a coordinate that does not satisfy the condition. Here, when expanding the area

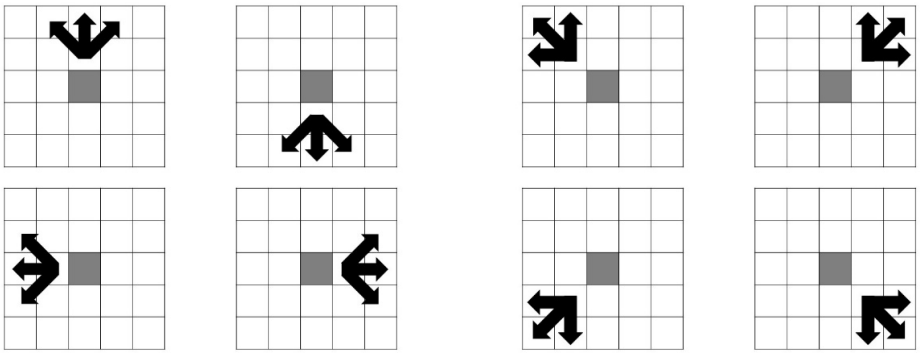

FIGURE 2. Region extension of the cell nucleus

of the cell nucleus, the maximum distance of expansion is limited to 16 pixels. This is an empirically obtained Manhattan distance based on the size of the cell nucleus. In the case of cell nucleus, those whose coordinates at 32×32 pixels did not fall within the central 24×24 pixels were judged as noise and excluded from the candidates. After the region is expanded, the region is labeled and a mask image is created. Mask processing is performed between the mask image and the input image, and a new ROI is created from which the cell nucleus region is cut out. If the area of the region is smaller than 5, the new ROI is not created and the pixel values in the region are changed to 0. The threshold value of the area within the region used to determine noise is an empirically determined value. Finally, the pixel values of the areas cut out as cell nuclei are changed to 0, and the process begins again with the creation of a gray-level histogram. This process is repeated until the maximum pixel value of the input image is set to 0.

3.2. **Identification of cell candidates.** The ROIs of the cell candidate regions obtained in the previous step are used for CNN identification [26]. In this paper, we used SqueezeNet [30]. Due to the small number of input images, the data has been expanded. The details are shown below.

There are two types of input images, CTCs, and other blood cells. Since the number of CTCs data used in this paper is very small (148), there is a bias in the data set. Therefore, we extended the CTCs dataset by using different combinations of red and blue images. For blood cells, unlike CTCs, we performed various transformation processes as other methods of data development, because different combinations of red and blue images may provide a representation of the characteristics of CTCs. Specifically, the input image was rotated up to 90 degrees and shifted or flipped randomly in the horizontal and vertical directions.

To identify CTCs using the detected cell candidate images, we constructed a CNN-based discriminator. In this paper, we have experimented with SqueezeNet [33]. SqueezeNet is a model that shows high discrimination performance with fewer parameters than AlexNet [34]. In this paper, the input image size is small (32×32 pixels), the classification target is not many classes but two classes (CTCs and non-CTCs), and overtraining may occur if the model layers are too deep, and the parameters are too large. Therefore, we used a model that could be trained efficiently with few parameters. The details are shown in Table 1.

4. **Result.** In this paper, we applied a processing for the identification of cell nucleus regions to the conventional method [27]. Table 2 shows the number of correctly detected CTCs and the number of over-detected non-CTCs after applying the proposed method to

Table 1. Structure of SqueezeNet

No.	Type	Size/ Stride	Output	Filters (1×1 squeeze)	Filters (1×1 expand)	Filters (3×3 expand)
0	Input	$-/-$	$32 \times 32 \times 3$	–	–	–
1	Convolution	$3 \times 3/1$	$32 \times 32 \times 96$	–	–	–
2	Fire	$-/-$	$32 \times 32 \times 128$	16	64	64
3	Fire	$-/-$	$32 \times 32 \times 128$	16	64	64
4	Add 2 and 3 layer	$-/-$	$32 \times 32 \times 128$	–	–	–
5	Fire	$-/-$	$32 \times 32 \times 128$	32	128	128
6	Max Pooling	$2 \times 2/2$	$16 \times 16 \times 256$	–	–	–
7	Fire	$-/-$	$16 \times 16 \times 256$	32	128	128
8	Add 6 and 7 layer	$-/-$	$16 \times 16 \times 256$	–	–	–
9	Fire	$-/-$	$16 \times 16 \times 384$	48	192	192
10	Fire	$-/-$	$16 \times 16 \times 384$	48	192	192
11	Add 9 and 10 layer	$-/-$	$16 \times 16 \times 384$	–	–	–
12	Fire	$-/-$	$16 \times 16 \times 512$	64	256	256
13	Max Pooling	$2 \times 2/2$	$8 \times 8 \times 512$	–	–	–
14	Fire	$-/-$	$8 \times 8 \times 512$	64	256	256
15	Add 13 and 14 layer	$-/-$	$8 \times 8 \times 512$	–	–	–
16	Batch Normalization	$-/-$	$8 \times 8 \times 512$	–	–	–
17	Activation (ReLU)	$-/-$	$8 \times 8 \times 512$	–	–	–
18	Global Average Pooling	$-/-$	$1 \times 1 \times 512$	–	–	–
19	Fully Connected (softmax)	$-/-$	$1 \times 1 \times 512$	–	–	–

Table 2. The result of detecting cells

Sample	GT	The proposed method		The conventional method [27]	
		Detected	Over-detected	Detected	Over-detected
No. 1	1	1	155	1	449
No. 2	13	13	117	13	434
No. 3	68	68	241	68	1,081
No. 4	16	16	350	16	916
No. 5	6	6	20	6	77
No. 6	44	44	42	44	281
Total	**148**	**148**	**925**	**148**	**3,238**

all the samples. Table 2 also shows the results obtained by using only the conventional method [27] against the proposed method. Here, in Table 2, GT is ground truth, which is the total number of CTCs in the images in each sample. For the number of correct answers in the same table, the *TPR* of both the proposed method and the conventional

TABLE 3. The result of segmentation algorithm

Sample	ROI including CTCs		ROI including non-CTCs	
	Before	After	Before	After
No. 1	1	1	155	250
No. 2	13	13	117	196
No. 3	68	68	241	365
No. 4	16	16	350	546
No. 5	6	6	20	51
No. 6	44	44	42	62
Total	**148**	**148**	**925**	**1,470**

method [27] is 100%. Following the results in Table 2, Table 3 shows the number of images immediately after the reconstruction of the blue image ROI by the proposed method. The size of the images in both Table 2 and Table 3 is 32×32 pixels.

Following the detection of cell candidate regions, we evaluated the identification accuracy of CTCs using the models of the proposed method and the comparison methods. The performance of the proposed method and the conventional method [27] was evaluated using *TPR* (true positive rate) [%] and *FPR* (false positive rate) [%] as evaluation indexes. The *TPR* and *FPR* used as evaluation indices are expressed by the following equations,

$$TPR = \frac{a}{a+b} \times 100[\%] \tag{10}$$

$$FPR = \frac{c}{c+d} \times 100[\%] \tag{11}$$

where a, b, c, and d in the above equations represent the number of candidate cell regions, and ground truth represents the correct answer data of CTCs in each sample. In this paper, the difference in area (number of pixels) between the correct and extracted regions is not considered in the evaluation because the performance is evaluated for each ROI.

In this paper, we evaluate the average performance of the models by using leave-one-out cross validation, where one sample is taken from the sample group as the test data and the other samples are used as the training data. Adaptive Moment Estimation (Adam) was used to optimize the training of each model. We set the initial learning rate to 0.01, the batch size to 128, and the maximum number of iterations to 20,000. The identification results for each model are shown in Table 4.

5. **Discussion.**

5.1. **Detection of cell candidates.** The results of the detection of cell candidate regions using the proposed method are shown in Table 2 and Table 3. From Table 2, the proposed method achieves about 71.4% reduction in the number of over-detected cells without decreasing the number of correct answers compared to the conventional method [27]. Figure 3 shows an example of the new images that can be excluded by the proposed method. The reason for the reduction in the number of over-detected non-CTCs is that we were able to exclude the cell candidate regions without cell nucleus reaction from the CTCs candidates in the blue image ROI, as shown in Figure 3. Here, it is not a problem to exclude cells that do not contain cell nucleus from the candidates because they are non-CTCs. Table 3 also shows that the number of ROIs containing CTCs could be increased without missing ROIs by identifying the cell nucleus region. This can be attributed to the fact that when multiple cell nucleus existed in the blue image ROI, multiple ROIs with

TABLE 4. The identification results for each model

(a) Proposed method

Sample	TPR[%]	FPR[%]	Number of detection	True positive	False negative	False positive	True negative
No. 1	0.0	4.0	251	0	1	10	240
No. 2	76.92	3.571	209	10	3	7	189
No. 3	91.18	4.658	433	62	6	17	348
No. 4	100.0	5.861	562	16	0	32	514
No. 5	50.00	3.922	57	3	3	2	49
No. 6	90.91	11.29	106	40	4	7	55
Average	88.51	5.102	269.7	21.8	2.833	12.5	232.5
Total	–	–	1,618	131	17	75	1,395

(b) Conventional method [27]

No. 1	100.0	2.004	450	1	0	9	440
No. 2	84.62	0.922	447	11	2	4	430
No. 3	97.06	3.978	1,149	66	2	43	1,038
No. 4	100.0	3.712	932	16	0	34	882
No. 5	100.0	3.896	83	6	0	3	74
No. 6	100.0	3.203	325	44	0	9	272
Average	97.30	3.150	564.3	24.0	0.667	17.0	522.6
Total	–	–	3,386	144	4	102	3,136

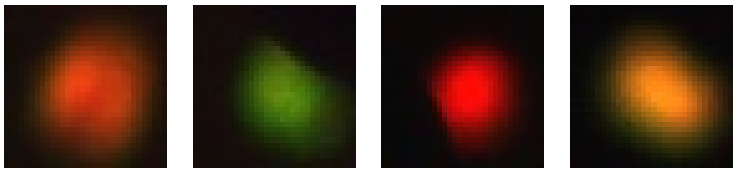

FIGURE 3. Examples of images that we were able to exclude

only one cell nucleus were created by reconstructing the ROI. Figure 4 shows an example of the identification of the cell nucleus region for a blue image ROI. Figure 4(a) shows the result of applying the cell nucleus region identification to the blue image, and Figure 4(b) shows the result of creating a color image by combining ROIs based on Figure 4(a). In Figures 4(a) and 4(b), the leftmost image shows the result of the conventional method [27], and the other images show the result of the proposed method for cell nucleus identification. On the other hand, there are some cases where the cell nucleus region extraction fails, as shown in Figure 5. Among these features are the presence of faint cell nucleus and cell fragments in the blue image ROI. The reason for the failure in identifying the cell nucleus region is that the segmentation algorithm only considers the concentration gradient in the eight directions from the largest pixel, resulting in difficulty in segmentation. To solve this problem, we need to revise the algorithm for cutting out the cell nucleus region, add more filters to emphasize the shapes close to the cell nucleus, and reset the conditions for expanding the cell nucleus region from the maximum pixel value. In addition, since the number of CTCs used in this paper is small (148), it is necessary to conduct experiments with additional samples to confirm the usefulness of the proposed method.

5.2. **Identification of cell candidates.** We trained SqueezeNet on the images resulting from the application of the proposed method to identify the CTCs, and obtained the

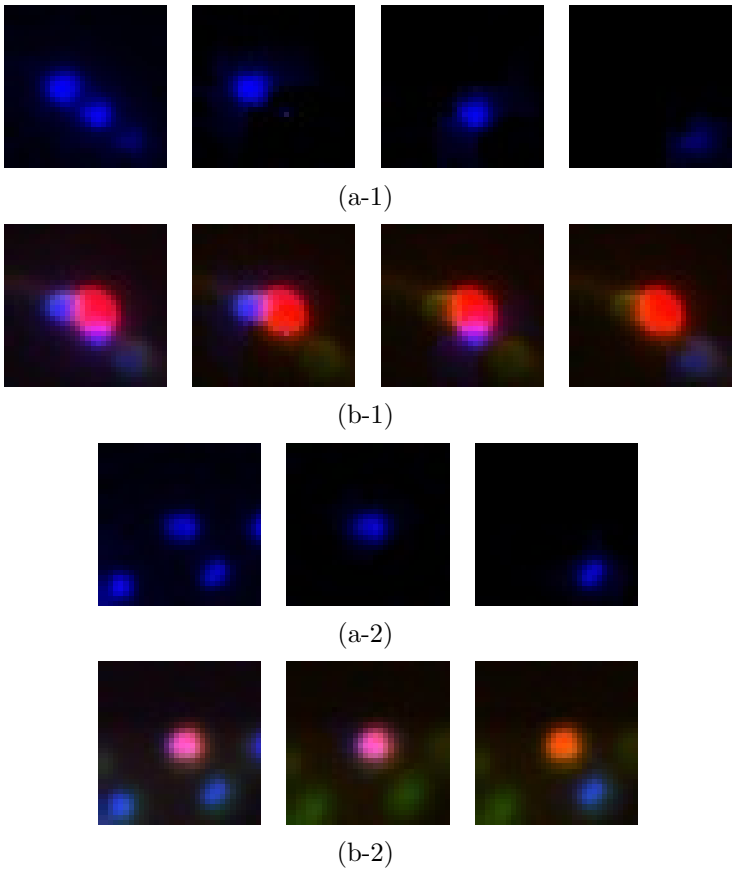

(a-1)

(b-1)

(a-2)

(b-2)

(a) The result of applying the process of cell nucleus region cropping to the blue image ROI
(b) The result of creating a color image by combining ROIs based on (a)

FIGURE 4. Results of nuclear cell identification

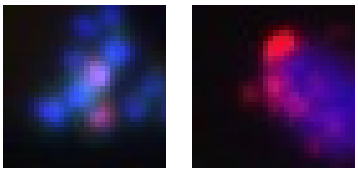

FIGURE 5. Example of identification failure about cell nucleus

results shown in Table 4(a). Figure 6 shows the images that were correctly identified by the proposed method. In Figure 6, the two images in 6(a) and 6(b) represent the same cell candidate region, where the left one is a CTC and the right one is a non-CTC. Figure 6 shows that even when the image is reconstructed by identifying the cell nucleus, it is possible to correctly identify whether the cell is a CTC or not. On the other hand, there are some cases of failure. Figure 7 shows an image that was incorrectly identified by applying the proposed method. The tendency is that the model misidentifies input images that contain light-colored cells and input images where the cytokeratin positive response is relatively stronger than the cell nucleus positive response. The reason for this may be that the model is greatly affected by the shading of the image. Furthermore, with the introduction of the Fire module, the number of parameters is reduced for efficient training, and some important parameters for discrimination may be missing.

Compared with the conventional method [27], the proposed method did not give good results in any of the evaluation metrics. One of the possible reasons for this is that the

(a) (b)

FIGURE 6. Examples of successful identification

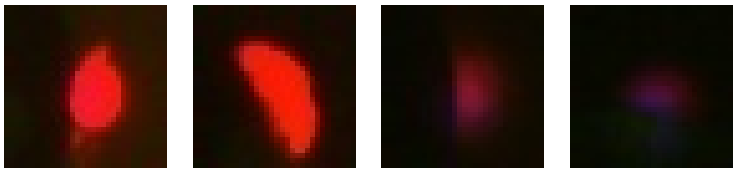

FIGURE 7. Example of identification failure

number of cell candidate regions was greatly reduced because of applying the proposed method in the detection stage, resulting in a decrease in the amount of data. Therefore, there may be a difference in the number of CTCs and non-CTCs in the training data during data expansion, resulting in a bias in the learning process, which may have prevented efficient learning. To solve these problems, we are going to consider new data expansion methods, normalization for image shading, and improvement of CNN layers. In addition, as in the discussion of detection, we need to analyze the results when more samples are added, and this is a future work.

6. **Conclusion.** In this paper, a CNN-based image analysis method is proposed for automatic detection of CTCs from fluorescence microscopy images to enable quantitative analysis by computer for the diagnosis of CTCs in blood. The process includes two steps: detection and identification. Firstly, we applied the selective enhancement filter and blob analysis to the red image to detect the cell candidate regions. Next, ROIs were cut out from the detected cell coordinates in each of the three-color images, and the ROIs were reconstructed by discriminating only the cell nucleus. After that, we constructed a CNN discriminator using the image generated by combining the three ROIs of each color as input. Due to the very small number of CTCs (148) in the blood, we performed a data expansion in which we trained different combinations of RGB data of CTCs. For non-CTCs, we extended the data by adding various transformations and trained them.

We applied the proposed method to 5,040 images of 6 samples to detect cell candidate regions and identify CTCs. As a result, the number of detections was 148 ($TPR = 100\%$) and the number of over-detections was 925. For discrimination, the SqueezeNet-based CNN model achieved $TPR = 88.51\%$ and $FPR = 5.102\%$. Compared with the conventional method [27], we succeeded in reducing the number of over detections by about 71.4% without losing the number of correct answers in detection, but there was no improvement in accuracy in discrimination. Future work includes further reduction of the number of over detects, investigation of new data expansion methods, and improvement of CNN layers. These improvements are expected to advance the development of a computer-aided diagnosis system to reduce the burden on doctors in CTCs analysis, which requires a great deal of time and effort.

REFERENCES

[1] World Health Organization, *The Problem of Cancer*, https://www.who.int/news-room/fact-sheets/detail/cancer, Accessed on 04-07, 2022.

[2] Ministry of Health, Labour and Welfare in Japan, *Composition of Major Causes of Death (2019)*, https://www.mhlw.go.jp/toukei/saikin/hw/jinkou/geppo/nengai19/dl/gaikyouR1.pdf, Accessed on 04-07, 2022.

[3] F. Tanaka, K. Yoneda and S. Hasegawa, Circulating tumor cells (CTCs) in lung cancer: Current status and future perspectives, *Lung Cancer (Auckl)*, vol.1, pp.77-84, 2010.

[4] K. Isobe, Y. Hata, K. Sato, T. Sano, K. Sugino, S. Sakamoto, Y. Takai and S. Honma, EGFR gene mutation detection using circulating tumor cells in peripheral blood, *Japanese Journal of Lung Cancer*, vol.51, no.6, pp.689-693, 2011.

[5] E. S. Lianidou and A. Markou, Circulating tumor cells in breast cancer: Detection systems, molecular characterization, and future challenges, *Clinical Chemistry*, vol.57, no.9, pp.1242-1255, 2011.

[6] Y. Chikaishi, K. Yoneda, T. Ohnaga and F. Tanaka, EpCAM-independent capture of circulating tumor cells with a 'Universal CTC-Chip', *Oncology Report*, vol.37, no.1, pp.77-82, 2017.

[7] K. Yoneda, T. Kuwata, Y. Chikaishi, M. Mori, M. Kanayama, M. Takenaka, S. Oka, A. Hirai, N. Imaishi, K. Kuroda, Y. Ichiki, T. Ohnaga and F. Taknaka, Detection of circulating tumor cells with a novel microfluidic system in malignant pleural mesothelioma, *Cancer Science*, vol.110, no.2, pp.726-733, 2019.

[8] E. Ozkumur, A. M. Shah, J. C. Ciciliano, B. L. Emmink, D. T. Miyamoto, E. Brachtel et al., Inertial focusing for tumor antigen-dependent and – Independent sorting of rare circulating tumor cells, *Science Translational Medicine*, vol.5, no.179, 179ra47, DOI: 10.1126/scitranslmed.3005616, 2013.

[9] K. Doi, Computer-aided diagnosis in medical imaging: Historical review, current status and future potential, *Computerized Medical Imaging and Graphics*, vol.32, nos.4-5, pp.198-211, 2007.

[10] L. L. Zeune, Y. E. Boink, G. van Dalum, A. Nanou, S. de Wit, K. C. Andree et al., Deep learning of circulating tumor cells, *Nature Machine Intelligence*, vol.2, pp.124-133, 2020.

[11] S. Wang, Y. Zhou, X. Qin, S. Nair, X. Huang and Y. Liu, Label-free detection of rare circulating tumor cells by image analysis and machine learning, *Scientific Reports*, vol.10, 12226, DOI: 10.1038/s41598-020-69056-1, 2020.

[12] Z. Guo, X. Lin, Y. Hui, J. Wang, Q. Zhang and F. Kong, Circulating tumor cell identification based on deep learning, *Frontiers in Oncology*, vol.12, 843879, DOI: 10.3389/fonc.2022.843879, 2022.

[13] A. Iyer, K. Gupta, S. Sharma et al., Integrative analysis and machine learning based characterization of single circulating tumor cells, *Journal of Clinical Medicine*, vol.9, no.4, 1206, DOI: 10.3390/jcm9041206, 2020.

[14] L. Timothy, T. Fredrik and K. Brian, Comparison and optimization of machine learning methods for automated classification of circulating tumor cells, *Cytometry Part A*, vol.89, no.10, pp.922-931, 2016.

[15] S. Carl, K. Solveigh, L. Jörg and F. Marc, Automated detection of circulating tumor cells with Naïve Bayesian classifiers, *Cytometry Part A*, vol.85, no.6, pp.501-511, 2014.

[16] N. Sedat, K. Deniz, E. Tuncay, H. S. Murat, K. Osman and E. Yavuz, Automatic segmentation, counting, size determination and classification of white blood cells, *Measurement*, vol.55, pp.58-65, 2014.

[17] M. Mohamed, B. Far and A. Guaily, An efficient technique for white blood cells nuclei automatic segmentation, *2012 IEEE International Conference on Systems, Man, and Cybernetics (SMC)*, pp.220-225, 2012.

[18] W. N. Tim, W. Heiko, S. Walter and R. Helge, A neural network architecture for automatic segmentation of fluorescence micrographs, *Neurocomputing*, vol.48, nos.1-4, pp.357-367, 2002.

[19] M. Xu, D. P. Papageorgiou, S. Z. Abidi, M. Dao, H. Zhao and G. E. Karniadakis, A deep convolutional neural network for classification of red blood cells in sickle cell anemia, *PLoS Computational Biology*, vol.13, no.10, e1005746, 2017.

[20] Y. Hafiyan, Afiahayati, R. Yanuaryska, E. Anarossi, V. M. Sutanto, J. Triyanto and Y. Sakakibara, A hybrid convolutional neural network-extreme learning machine with augmented dataset for DNA damage classification using comet assay from buccal mucosa sample, *International Journal of Innovative Computing, Information and Control*, vol.17, no.4, pp.1191-1201, 2021.

[21] P. Saichua and O. Surinta, Comparative study between ensemble and fusion convolutional neural networks for diabetic retinopathy classification, *ICIC Express Letters*, vol.16, no.4, pp.401-408, 2022.

[22] M. Toratani, M. Konno, A. Asai et al., A convolutional neural network uses microscopic images to differentiate between mouse and human cell lines and their radioresistant clones, *Cancer Res.*, vol.78, no.23, pp.6703-6707, 2018.
[23] L. Zhang, L. Lu, I. Nogues, R. M. Summers, S. Liu and J. Yao, DeepPap: Deep convolutional networks for cervical cell classification, *IEEE Journal of Biomedical and Health Informatics*, vol.21, no.6, pp.1633-1643, 2017.
[24] C. L. Chen, A. Mahjoubfar, L. C. Tai, I. K. Blaby, A. Huang, K. R. Niazi and B. Jalali, Deep learning in label-free cell classification, *Scientific Reports*, vol.6, no.1, pp.1-16, 2016.
[25] K. Tsuji, H. Lu, J. K. Tan, H. Kim, K. Yoneda and F. Tanaka, Detection of circulating tumor cells in fluorescence microscopy images based on ANN classifier, *Mobile Networks and Applications*, vol.25, pp.1042-1051, 2020.
[26] K. Nakamichi, H. Lu, H. Kim, K. Yoneda and F. Tanaka, Classification of circulating tumor cells in fluorescence microscopy images based on SqueezeNet, *2019 19th International Conference on Control, Automation and Systems (ICCAS)*, pp.1042-1045, 2019.
[27] K. Nakamichi, H. Lu, H. Kim, K. Yoneda and F. Tanaka, Automatic detection of CTC in fluorescence microscopy images by using SqueezeNet, *The Journal of the Institute of Image Electronics Engineers of Japan: Visual Computing, Devices & Communications*, vol.49, no.2, pp.136-143, 2020 (in Japanese).
[28] Leica, *Products*, https://www.leica-microsystems.com/products/light-microscopes/p/leica-dmi8-id/, Accessed on 09-08, 2021.
[29] D. H. Hubel and T. N. Wiesel, Receptive fields of single neurones in the cat's striate cortex, *The Journal of Physiology*, vol.148, no.3, pp.574-591, 1959.
[30] Q. Li, S. Sone and K. Doi, Selective enhancement filters for nodules, vessels, and airway walls in two- and three-dimensional CT scans, *Medical Physics*, vol.30, no.8, pp.2040-2051, 2003.
[31] T. Lindeberg, Detecting salient blob-like image structures and their scales with a scale-space primal sketch: A method for focus-of-attention, *International Journal of Computer Vision*, vol.11, no.3, pp.283-318, 1993.
[32] S. Weissbach and F. Wyrowski, Error diffusion procedure: Theory and application in optical signal processing, *Applied Optics*, vol.31, no.14, pp.2518-2534, 1992.
[33] F. N. Iandora, S. Han, M. W. Moskewics, K. Ashraf, W. J. Dally and K. Keutzer, SqueezeNet: AexNet-level accuracy with 50x fewer parameters and $<$ 0.5MB model size, *arXiv Preprint*, arXiv: 1602.07360, 2016.
[34] K. Alex, I. Sutskever and G. E. Hinton, ImageNet classification with deep convolutional neural networks, *Communications of ACM*, vol.60, no.6, pp.84-90, 2017.

Author Biography

Kazuki Hashimoto received the B.Sc. degree from Kyushu Institute of Technology, Japan, 2021. He is studying at Kyushu Institute of Technology, Japan. His main research interests are image processing and artificial intelligence.

Tohru Kamiya received his B.A. degree in electrical engineering from Kyushu Institute of Technology in 1994, the Master's and Ph.D. degree from Kyushu Institute of Technology in 1996 and 2001, respectively. He is a professor in the Department of Control Engineering at Kyushu Institute of Technology. His research interests are focused on medical application of image analysis. He is currently working on automatic segmentation of multi-organ of abdominal CT image, and temporal subtraction of thoracic MDCT image sets.

Guangxu Li received his B.A. and Master degree in automatic control engineering from Liaoning University of Technology in 2006 and 2009 respectively, and the Ph.D. degree from Kyushu Institute of Technology in 2013. He is an associate professor in the School of Electronics and Information Engineering at Tiangong University. His research interests are focused on medical application of computational geometry. He is currently working on images processing and analysis on ophthalmological OCT images, especially the vessel-like structures.

Kazue Yoneda received Ph.D. degree and is an assistant professor of Omics Medicine at Hyogo Medical University, Japan. Her research focuses on blood biomarkers for cancer diagnosis. She conducted research on circulating tumor cells (CTCs) in thoracic malignancy at the University of Occupational and Environmental Health, Japan from 2013 to 2020.

Fumihiro Tanaka received M.D. & Ph.D. degrees and is the professor and director of the Second Department of Surgery (Chest Surgery), University of Occupational and Environmental Health, Japan. He is working as a thoracic surgeon at the University Hospital, and also conducting a variety of translational research on thoracic malignant diseases including lung cancer and malignant pleural mesothelioma.